Environmental Science Nano

ROYAL SOCIETY OF CHEMISTRY

PAPER

View Article Online
View Journal | View Issue

Cite this: *Environ. Sci.: Nano*, 2020, 7, 1539

Characterization of aerosolized particles from nanoclay-enabled composites during manipulation processes†

Eun Gyung Lee, ‡*[a] Lorenzo Cena,[b] Jiwoon Kwon,[c] Ali Afshari,[a] HaeDong Park,[b] Gary Casuccio,[d] Kristin Bunker,[d] Traci Lersch,[d] Ashley Gall,[e] Huy Pham,[e] Alixandra Wagner,[e] Sushant Agarwal,[e] Cerasela Zoica Dinu,[e] Rakesh Gupta,[e] Sherri A. Friend[a] and Todd A. Stueckle ‡[a]

Received 23rd October 2019,
Accepted 26th March 2020

DOI: 10.1039/c9en01211g

rsc.li/es-nano

Manufacturing, processing, use, and disposal of nanoclay-enabled composites potentially lead to the release of nanoclay particles from the polymer matrix in which they are embedded; however, exposures to airborne particles are poorly understood. The present study was conducted to characterize airborne particles released during sanding of nanoclay-enabled thermoplastic composites. Two types of nanoclay, Cloisite® 25A and Cloisite® 93A, were dispersed in polypropylene at 0%, 1%, and 4% loading by weight. Zirconium aluminum oxide (P100/P180 grits) and silicon carbide (P120/P320 grits) sandpapers were used to abrade composites in controlled experiments followed by real-time and offline particle analyses. Overall, sanding the virgin polypropylene with zirconium aluminum oxide sandpaper released more particles compared to silicon carbide sandpaper, with the later exhibiting similar or lower concentrations than that of polypropylene. Thus, a further investigation was performed for the samples collected using the zirconium aluminum oxide sandpaper. The 1% 25A, 1% 93A, and 4% 93A composites generated substantially higher particle number concentrations (1.3–2.6 times) and respirable mass concentrations (1.2–2.3 times) relative to the virgin polypropylene, while the 4% 25A composite produced comparable results, regardless of sandpaper type. It was observed that the majority of the inhalable particles were originated from composite materials with a significant number of protrusions of nanoclay (18–59%). These findings indicate that the percent loading and dispersion of nanoclay in the polypropylene modified the mechanical properties and thus, along with sandpaper type, affected the number of particles released during sanding, implicating the cause of potential adverse health effects.

Environmental significance

Nanoclay-enabled polymer composites are used in a variety of emerging applications ranging from food packaging, automotive materials, medical devices, *etc.* The life cycle of the nanocomposites could lead to the release of nanoclay particles from the base material they are embedded in. However, occupational exposures are poorly understood. Here, we characterized the aerosolized particles from nanoclay composites during sanding by varying percent nanoclay loading, surface organic coating type, sandpaper type, and sandpaper grit sizes. The results indicate that the inclusion of nanoclay in polypropylene has an effect on the matrix structure and the rate of degradation of the material. The findings can be extended to address unknown pulmonary risks associated with use of nanoclay-enabled composites along their life cycle.

Introduction

Two-dimensional nanoclays are naturally occurring, fine-grained, layered aluminosilicate crystalline structures. Since they are widely available, inexpensive and environmentally friendly, their potential to improve the mechanical strength, thermal stability, and barrier properties in polymer matrices have been extensively investigated over the past few decades.[1] As a result, nanoclay-enabled nanocomposites continue to rapidly emerge on the global market in novel applications including food and beverage packaging, biomedical tools,

[a] *National Institute for Occupational Safety and Health (NIOSH), Health Effects Laboratory Division (HELD), 1095 Willowdale Road, Morgantown, WV 26505, USA. E-mail: dtq5@cdc.gov; Tel: +1 304 285 6041*
[b] *West Chester University, West Chester, PA, USA*
[c] *Korea Occupational Safety and Health Agency, South Korea*
[d] *RJ Lee Group, Monroeville, PA, USA*
[e] *Chemical and Biomedical Engineering, West Virginia University, Morgantown, WV, USA*

† Electronic supplementary information (ESI) available. See DOI: 10.1039/c9en01211g

‡ Contributed equal to this work.

cosmetics, catalysis, textiles, aqueous barriers, fire retardants, and the automobile/aerospace parts industry.[1–6] Of the many types of nanoclays, montmorillonite (MMT) is one of the common layered aluminosilicate nanofillers applied to a wide range of applications because of the well-reported physical and chemical properties.[1] Prior to integration in polymer matrices, hydrophilic MMT is modified with an organic modifier coating (*e.g.*, quaternary ammonium tallow compounds), to increase interactions (*e.g.*, surface functionality and spacing) with hydrophobic polymers[7,8] currently used for such applications.

The implementation of nanoclays into commercial and industrial products triggered extensive evaluation of their toxicological profiles. Previous studies have found adverse effects upon exposures to raw nanoclay materials and/or organomodified nanoclays that include pulmonary health effects (*e.g.*, respiratory tract irritation), hemolysis, cytotoxicity effects (*e.g.*, decreased cellular proliferation), mitochondrial and membrane damage, reactive oxygen species generation, and genotoxic effects.[9–31]

The life cycle of nanocomposites involves manufacturing, machining, distribution, use, and disposal/recycling processes. These activities could lead to potential worker inhalation exposure to aerosolized engineered nanomaterials (ENMs) due to the release of nano-sized particles or particles with protruding ENMs from a nanocomposite material, which potentially harbors health risks. For several ENM fillers, exposures from various mechanical manipulations of nanocomposites have been studied to a moderate extent including sanding, cutting, grinding, shredding, and drilling with nanocomposite materials (*e.g.*, carbon nanotubes (CNT)-, carbon nanofiber-, zinc oxide-, and iron oxide-enabled organic polymers).[32–35] Among nanocomposites reported in the previous studies, only a few studies assessed exposures to aerosolized particles from handling nanoclay-enabled composites using mechanical manipulation. Examples include a shredding task with a polypropylene (PP) resin and PP resin reinforced with MMT nanoclay (5% by weight),[36] mechanical drilling of polyamide (PA)-6 and PA-6 integrated with organically modified MMT (5% by weight),[37] mixing nanoclay particles (Cloisite® 20A) with ethylene vinyl acetate polymer,[38] and sanding three different materials (PET, PET coated with a polyvinylchloride [PVC] layer, and PET coated with a PVC layer containing nanoclays [type of clay and percent not specified]) using a Taber Abraser test method.[39] These studies reported ultrafine and fine particle release during composite synthesis, machining, and manipulation. However, little attention was paid to how changes in physicochemical properties of the intact nanocomposite, such as percent nanoclay loading, dispersion, and strength, or in the manipulation process contributes to the number, size, and chemistry of the released airborne particulate.

Aerosolization of nanoclay-enabled composite particles in occupational settings during manipulations has been forecasted as a potential occupational hazard in the near future.[35] Compared to other high exposure hazard ENM-enabled composites, inadequate information exists on nanoclay pulmonary health risks compared to other ENMS, including carbon nanotubes. To the best of our knowledge, limited information exists for pulmonary toxicological effects associated with organomodified nanoclay (ONC) exposure along their life cycle. For example, Stueckle *et al.*[31] conducted toxicity assessment using pre- and post-incinerated ONC in mice. ONC was reported to induce a low, persistent inflammatory signal with indications of potential pro-fibrotic effect while incinerated nanoclays produced less pulmonary inflammation and granuloma formation compared to that of pristine MMT. There is a significant gap for investigating real world exposure scenarios, the physicochemical properties of nanocomposites that drive exposure hazard, and the impact on worker health across the nanoclay-enabled composite life cycle.

Thus, the current study was conducted to characterize airborne particles released during a machining process of nanoclay-enabled thermoplastic composites and relating these findings to the physicochemical properties of the as-produced nanocomposite. We hypothesized that differences in percent loading, organic modifier coating, dispersion, and machining process would change aerosolized dust chemistry, particle number, and size distributions. Of the various mechanical manipulations, we selected a sanding task, which is a common and growing practice in manufacturing industries.[40] These laboratory controlled studies will serve to directly test what physicochemical properties of nanoclay-enabled thermoplastic composites increase airborne hazards and address unknown pulmonary risks associated with use of nanoclay-enabled composites along their life cycle.

Methods

Nano-enabled composite materials

Polypropylene (PP; Amoco BP 1246) was selected as a model virgin thermoplastic material. This material was chosen because PP-nanoclay composites are being used extensively in making durable agricultural film, packaging film, and automotive panels.[41] Two types of nanoclay, Cloisite® 25A and Cloisite® 93A (Southern Clay Products, Gonzalez, TX) at 1% and 4% of concentration by weight, were embedded into the PP *via* melt mixing and thermal compression molding using a metal frame built in-house. Detailed information of making nanoclay composite blocks is provided in ESI† method A. Virgin PP (0% nanoclay) served as a comparative control of non-ENM-enabled thermoplastic composite. Cloisite 25A is a MMT modified with dimethyl, dehydrogenated tallow, 2-ethylhexyl quaternary ammonium and Cloisite 93A is another MMT modified with methyl, dehydrogenated tallow ammonium. The chemical structures of both Cloisites are presented in ESI† Fig. S1. For each nanoclay-enabled PP composite and virgin PP, we made 8 uniform blocks per batch measuring 10 cm (width) by 15 cm (height) by 0.3 cm (depth).

Characterization of mechanical properties

For each composite material (virgin PP and all nanoclay-enabled composites), mechanical properties including Young's modulus, tensile strength, toughness, and elongation at break were determined as previously described in Wagner *et al.*[42] Crystallinity was determined with a PANalytical X'Pert Pro XRD (Malvern PANalytical, Royston, UK) using a Cu-Kα_1 8047.2 eV source at 45 kV and 40 mA. In addition, the degree of dispersion of nanoclay within the PP matrix was evaluated with a Bruker D8 discovery X-ray diffractometer (XRD) (Bruker, Madison, WI) by determining exfoliation (*i.e.*, the separation distance between the embedded nanoclay platelets). Finally, visualization of dispersed nanoclay within the PP matrix of each composite material was performed *via* a transmission electron microscopy (TEM) analysis. Detailed information on bulk composite mechanical property, crystallinity, and nanoclay dispersion characterization is provided in ESI† method B.

Particle generation

Sanding particles of nanocomposites and virgin materials were generated using the same automated, controlled exposure chamber built for a previous study[40] with a modification of the air inlet location (Fig. 1). The air was extracted at a flow rate of 18 L min^{-1} and high-efficiency particulate air filters were placed at the air inlet and outlet ports. A sander (model 97181, Central Machinery, Camarillo, CA) was modified by placing the motor outside the chamber and fitted with a 10.2 cm by 91.4 cm sanding belt operated at constant speed of 1150 ft min^{-1}. The material holder included a 252 g weight to provide constant force during sanding. Two types of sandpapers, zirconium aluminum oxide (R823P, Norton, Saint-Gobain Abrasives, Inc., Worcester, MA) with P100 and P180 grits and silicon carbide (R422, Norton) with P120 and P320 grits, were employed.

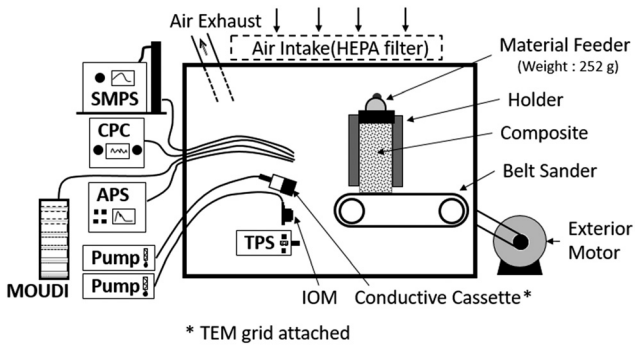

Fig. 1 Experimental setup for automated sanding system (resource: modified from Fig. 1 by Kang *et al.*[40]). This figure was published in *NanoImpact*, J. Kang, A. Erdely, A. Afshari, G. Casuccio, K. Bunker, T. Lersch, M. M. Dahm, D. Farcas, L. Cena, Generation and characterization of aerosols released from sanding composite nanomaterials containing carbon nanotubes, **5**, 41–50, Copyright Elsevier (2017).

During the sanding, an area of 3.0 cm^2 of the composite blocks was in contact with the sanding belt.

Airborne particle measurements

Particles released during sanding were measured with direct-reading instruments (DRIs) placed outside the chamber by drawing air *via* conductive silicon tubing. The distance between the inlets of the tubing and the sander was approximately 20 cm (Fig. 1). The DRIs included 1) condensation particle counter (CPC, model 3775, TSI Inc., Shoreview, MN) to measure total particle number concentration every second at 1.5 L min^{-1} (measurable size range of 0.004–3 μm), 2) scanning mobility particle sizer (SMPS, model 3080, TSI Inc.) to measure particle number and mass concentrations based on the size distribution every 2 min 15 s at 0.6 L min^{-1} (size range of 9.8–414.2 nm), and 3) aerodynamic particle sizer (APS, model 3321, TSI Inc.) to measure particle size distributions by number and mass every minute at 5 L min^{-1} (size range of 0.5–20 μm).

A micro orifice uniform deposition impactor (MOUDI; model 100, MSP Corporation, Shoreview, MN) was placed outside the chamber and run at 30 L min^{-1} to determine mass distributions. Each stage was loaded with 47 mm aluminum foil filter except for the filter stage loaded with polyvinylchloride filter (0.4 μm pore size). The collection stages of the MOUDI were analyzed gravimetrically using a microbalance (model XP 64, Mettler-Toledo, LLC, Columbus, OH) in an environmentally controlled weighing chamber.

Airborne particles released during sanding were collected with an inhalable sampler (IOM, SKC Inc., Eighty Four, PA, USA) loaded with polycarbonate (PC) filter (25 mm filter with 0.4 μm pore size) at a flow rate of 2.0 L min^{-1} for electron microscopy (EM) analysis. In addition, a thermophoretic sampler (TPS100, RJ Lee Group, Monroeville, PA), capable of collecting particles directly on a TEM grid, was placed in the chamber to collect particles in the range of approximately 10–300 nm based on thermal precipitation.[43] Lastly, airborne particles were directly collected on two TEM grids attached to a mixed cellulose ester membrane filter (25 mm filter with 0.8 μm pore size, SKC Inc.) placed in a conductive cowl sampler at a flow rate of 2.0 L min^{-1} for EM analysis.

Chamber measurements

Prior to starting the sander, background measurements were collected for 7 min with the DRIs. The off-line samplers were not operated at this time. After completing the background measurements, the sander was turned on and a sample block was placed down towards the sander under weight, which started the sanding work. The TPS100 and sampling pumps connected to the MOUDI, inhalable sampler, and conductive sampler were operated as the sanding started. Particle concentrations were allowed to stabilize inside the chamber for 8 min and DRI measurements followed for 15 min. After cleaning the chamber with a vacuum, a new sandpaper belt was loaded and the test was repeated. For each material and

sandpaper type, three replicates were conducted. After completing three replicates, the chamber was thoroughly vacuumed and wiped with laboratory-grade wipes to prevent cross-contamination from the previous test. The tests were then repeated with either a different sandpaper type and/or a different composite block.

For each test condition, the temperature on the surface where a composite block contacted the sandpaper was measured twice, after 9 minute and 22 minutes of sanding, with a traceable infrared thermometer (model 06664254, Fisher Scientific, Pittsburgh, PA) to determine any changes during the sanding work. In addition, the height of each material was measured pre- and post-sanding work to determine the amount of material abraded after sanding. For the TPS100 and samplers loaded with filter, cumulative samples were collected for three replicates to collect sufficient amount of aerosolized particles, while DRIs collected data for the 7 min background measurements and 15 min sanding periods.

Electron microscopy analysis

To assist in positively identifying protruded or embedded nanoclay in collected airborne particles, as-prepared nanoclays and slivers of PP1246 were suspended in water with light sonication, followed by a 1 : 10 dilution and filtration onto PC filters with 0.4 μm pores.[31] The filters were assessed for their elemental composition using a field-emission scanning electron microscope (FESEM; Hitachi S-4800, Hitachi High Technologies America, Schaumburg, IL) coupled with energy dispersive X-ray spectroscopy (EDS) analysis. It revealed that both as-produced nanoclays displayed spectra of Si, Al, C, O, with occasional Mg and Fe. The ratio of carbon to oxygen and the presence of a trace amount of Si and Al was consistent overall among the composite particles along with the distinct morphological features. Slivers of PP1246 were evaluated for incidental particles or metal contamination and routinely showed only C and O signatures.

In addition, sandpaper dust was generated by rubbing two sandpaper belts together without the block of composite material to differentiate the sandpaper dust from the composite particles. The dust was then dispersed by suspending in isopropanol, and depositing the suspension on a PC filter. The prepared PC filter was examined for the individual particles ≥1 μm using a FESEM (MIRA3, Tescan USA, Warrendale, PA) equipped with computer-controlled scanning electron microscopy (CCSEM, RJ Lee Group) analysis software (IntelliSEM) for automated particle analysis. We limited the detailed evaluation to particles ≥1 μm based on the previous finding that most particles from mechanical processes (*e.g.*, sanding) are in the micrometer size.[44]

Subsections of each PC filter loaded in IOM were also analyzed by CCSEM methods for particles ≥1 μm by obtaining a secondary electron image and EDS. For each composite material, about 3000–5000 particles were captured. Diameter measurements and stage coordinates were documented to re-locate the particles following the analysis. Criteria were developed to sort composite and sandpaper particles based on our preliminary work comparing particles' morphology and elemental compositions. First, the CCSEM particle data was sorted by elemental composition. Next, the FESEM images collected during the CCSEM analysis of the carbonaceous particles were visually examined for composite particle morphological characteristics. Then, for particles indicative of composite materials, elemental spectra were reviewed for trace levels of characteristic nanoclay elements (Al–Si). Finally, the potential composite particles were relocated to confirm the composite particle classification and to examine the surface of the particles for nanoclay protrusions. Criteria applied to establish particle classification are described in detail in ESI† method C and Table S1. For each filter, at least 200 composite particles were examined manually for the presence of nanoclay protrusions. The number of composite particles with Al–Si platelets protruding from the surface of the particle were counted to determine their relative concentrations in each sample. A total of 200 particles is recommended by the National Institute of Standards and Technology[45] for statistical significance. For cost-saving purposes, only the filters with P100 sandpaper showing considerably higher particle number concentrations were analyzed *via* CCSEM.

The TEM grids collected from the TPS100 were examined manually with a FESEM with scanning transmission electron microscopy capabilities (FESEM/STEM, S-5500, Hitachi High Technologies America) equipped with EDS to assess the potential release of nanoclay particles. In addition, TEM grids attached to a mixed cellulose ester membrane filter placed in a conductive cowl sampler were examined with a JEOL 1400 TEM (model 1400, JEOL Inc.) at 80 kV.

Data analysis

Data collected with DRIs were averaged from the three replicates and adjusted by subtracting the background concentrations. Total particle number concentrations were calculated by combining the CPC and APS data. The size-selective particle number concentrations were obtained from the SMPS and APS. A linear interpolation method after converting the APS aerodynamic diameter to the corresponding physical diameter was used to avoid discontinuities of particle concentrations between the maximum and minimum cut-off diameter of SMPS and APS, respectively. Although the MOUDI was intended to be used to determine particle mass concentration, almost all particles collected only on the first stage with a cut-off diameter of 18.4 μm. Respirable mass (RM) concentrations were calculated using CPC and APS data following Peters *et al.*:[46]

$$\mathrm{RM} = \frac{\pi}{6} d_{\mathrm{CPC}}{}^{3} \rho N S_{\mathrm{R}}(d_{\mathrm{CPC}}) + \sum_{i=1}^{51} \frac{\pi}{6} d_{\mathrm{APS},i}{}^{3} \rho N_{\mathrm{APS},i} S_R(d_{\mathrm{APS},i}) \quad (1)$$

where, d_{CPC} is the midpoint diameter of the CPC, calculated as 120 nm slip-corrected aerodynamic diameter with a shape factor of 1.36 for irregular particles determined by

morphological examination *via* electron microscopy,[44] and particle diameter range of 5 nm to 3 μm, ρ is the particle density of the virgin PP material (0.855 g cm^{-3}), N is the number concentration measured by the CPC, S_R is a function for the fraction of respirable mass,[47] $d_{APS,i}$, is the midpoint diameter of the APS channel i, and $N_{APS,i}$ is the number concentration measured by the APS for a given size channel i. The first 19 channels of the APS were omitted from the data as they overlapped the size range of the CPC.

Statistical analysis was performed to compare the particle number and respirable mass concentrations among different composites and between sandpaper grit sizes using SAS/STAT software (version 9.3, SAS Institute Inc., Cary, NC). The nonparametric Kruskal–Wallis test was performed followed by Tukey Kramer honestly significant difference for the comparisons. A p-value of 0.05 was used for testing statistical differences.

For the CCSEM data review, the results of particle elemental composition by number and weight percent and size distribution frequency by number and weight were reported for each composite material. The size distribution frequency by weight was obtained as described by Kang *et al.*[40]

Results

1. Characterization of mechanical properties

Overall, the tensile strength and toughness for 1% 25A-PP, 1% 93A-PP, and 4% 93A-PP was higher than that of 4% 25A-PP and PP (Table 1). All composites displayed similar elasticity (*i.e.*, Young's modulus) and elongation at break except for the 4% 25A composite; a considerably lower modulus value for the 4% 25A-PP compared to others contributed to a significant increase in elongation at break during testing. These results indicated that 4% 25A-PP potentially possessed differences in composite crystal structure or dispersion of the nanoclay within the matrix compared to the other nanoclay-enabled composites. A summary of graphical presentation of mechanical properties is reported in ESI† Fig. S2.

The XRD crystallinity pattern for PP1246 was characteristic to that of the isotactic α-form of PP (ESI† Fig. S3).[48,49] Similar diffraction patterns were also obtained for 4% 93A-PP and 4% 25A-PP with a few tenths of degree shifts for some peaks to lower 2θ angles, which could be attributed to the roughness of the films examined or chemical modifications resulting in changes in the structure. These results indicate that the nanoclay composites retain a PP crystal structure.

As shown in Fig. 2A, the virgin PP exhibited a broad, low intensity peak between 2θ of 1 to 2.4°, indicating an absence of particle filler material, while both 4% 25A-PP and 4% 93A-PP displayed peaks within this range. It is known that neat Cloisite 25A and Cloisite 93A showed peaks at 4.8° (indicating a d-spacing of 1.86 nm) and 3.8° (d-spacing of 2.36 nm), respectively.[1,50,51] Cloisite 25A composite showed a sharp peak at 1.9° (d-spacing 4.72 nm) and a broad peak between 2.4° and 4.3° peaking at 3.5° (d-spacing 2.56 nm) while Cloisite 93A composite displayed a peak at 3.1° (d-spacing 2.89 nm) bounded by 2.5° and 3.7°. These data suggest that Cloisite 25A composite displayed intercalated (*i.e.*, partial separation of the interlayers of a nanomaterial) while Cloisite 93A composite exhibited a mix of exfoliated (*i.e.*, the separation of the interlayers of a nanomaterial) and stacked platelets.[6,52–54] Additionally, the lower intensity of 4% 93A-PP compared to that of 4% 25A-PP, presumably, suggests less agglomeration with the PP matrix.[54] Cloisite 93A appears to have a higher affinity for PP relative to Cloisite 25A, resulting in a better dispersion, as indicated by the presence of only 1 peak for 4% 93A-PP.[6,53,55] Generally, a larger d-spacing, as is present for Cloisite 93A relative to Cloisite 25A,[1] allows a better dispersion of interlayers compared to a smaller d-spacing.[51] Subsequent TEM analysis confirmed that the Cloisite 93A (4% w/w) dispersed better than the Cloisite 25A (4% w/w) (Fig. 2B). Similar trends were observed in 1% nanoclay-enabled PP wherein stacks of Cloisite 25A platelets were still highly visible in TEM imaging. Sectioned virgin PP material showed little to no presence of incidental particles within the matrix.

Table 1 Summary of nanoclay-enabled polypropylene composite materials, sandpaper grit, particle number and respirable mass concentrations, and mechanical properties

Material ID	Composites	Sand paper grit	Average number concentration (SE) (particles per cm^3)	Respirable mass concentration (SE) (μg m^{-3})	Tensile strength (SE) (MPa)	Elongation at break (SE) (mm)	Toughness (SE) (J m^{-3})	Young's modulus (SE) (Gpa)
PP	Polypropylene (PP) (virgin)	P100	45 914 (976)	40.1 (0.9)	18.1 (2.2)	4.5 (1.1)	324 020 (78	1.32
		P180	11 169 (222)	10.4 (0.3)			252)	(0.09)
1% 25A-PP	Cloisite 25A-PP (1% w/w)	P100	69 824 (948)	60.6 (0.8)	28.2 (0.8)	3.8 (0.4)	620 149 (39	1.13
		P180	22 481 (214)	21.8 (0.3)			378)	(0.05)
4% 25A-PP	Cloisite 25A-PP (4% w/w)	P100	43 221 (368)	35.6 (0.4)	13.7 (1.7)	8.0 (1.1)	318 351 (85	0.88
		P180	14 490 (145)	12.8 (0.1)			147)	(0.07)
1% 93A-PP	Cloisite 93A-PP (1% w/w)	P100	67 471 (478)	54.0 (0.3)	26.0 (1.0)	5.3 (0.9)	670 356 (85	1.28
		P180	23 388 (422)	20.7 (0.4)			117)	(0.06)
4% 93A-PP	Cloisite 93A-PP (4% w/w)	P100	60 900 (971)	49.3 (0.7)	24.4 (0.5)	3.7 (0.9)	448 494 (42	1.45
		P180	28 943 (436)	23.7 (0.3)			599)	(0.09)

SE = standard error.

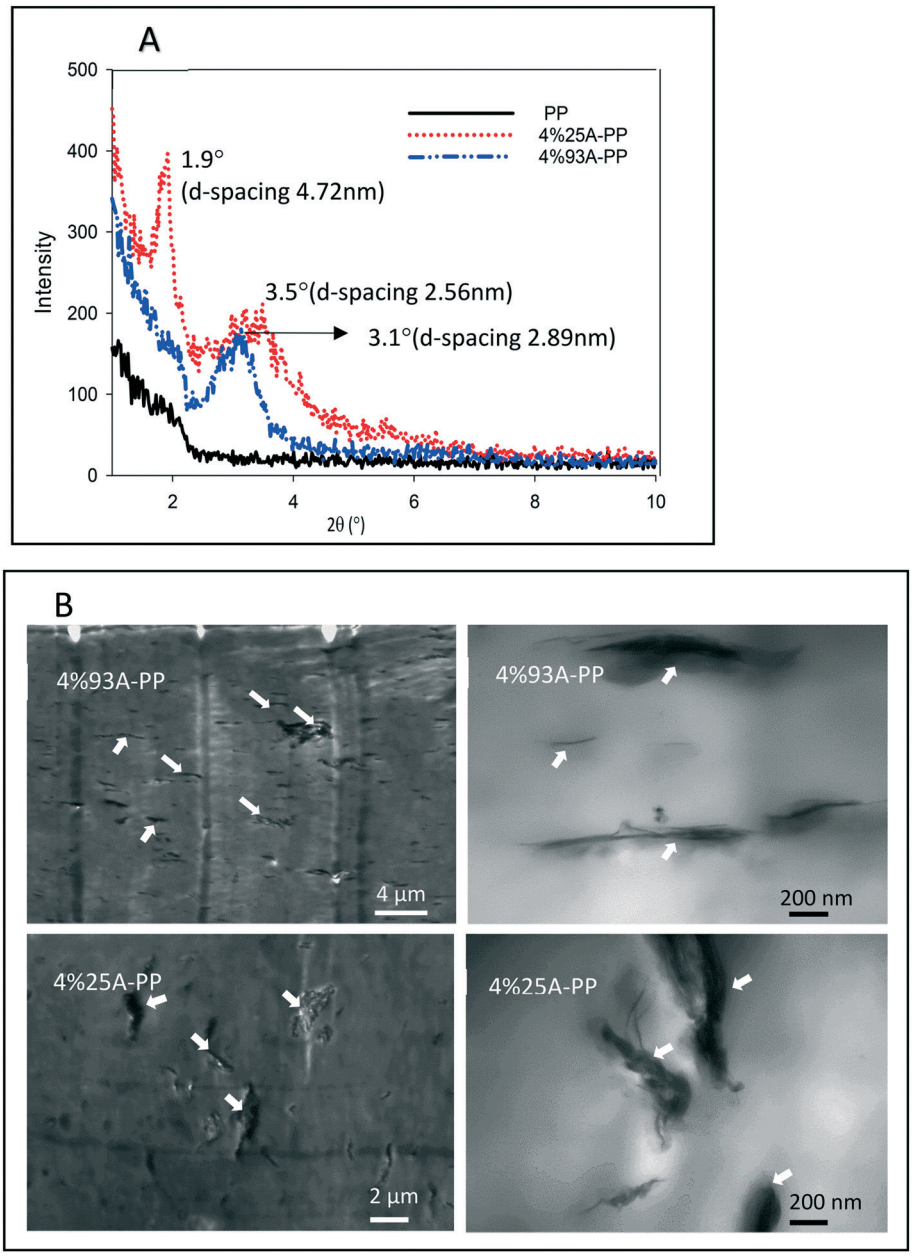

Fig. 2 Dispersion characteristic of nanoclay-enabled polypropylene (PP) composites compared to virgin PP determined *via* X-ray diffraction (A) and TEM images of 4% 93A-PP and 4% 25A PP showing dispersion and spacing of nanoclay platelets (white arrows) within the polypropylene matrix (B). The 4% 93A composite showed greater spacing and dispersion between nanoclay platelets while 4% 25A composite showed intercalated and agglomerated nanoclay platelet stacks and less-well dispersed platelets. Dark areas indicate dense inorganic material (*i.e.,* nanoclay) while lighter areas indicate polymer matrix.

2. Airborne particle measurements using direct-reading instruments

2.1 Effects of sandpaper grit. Overall, sanding virgin PP with zirconium aluminum oxide sandpaper released more particles than sanding with silicon carbide sandpaper. In addition, when sanded with silicon carbide sandpaper, the particle number concentrations of nanocomposites were similar or lower than the virgin PP except for 1% 25A-PP (ESI† Table S2). Thus, a further investigation including characterization of nanoclay-enabled composites and EM analysis was conducted for the samples collected using the zirconium aluminum oxide sandpaper.

In general, P100 sandpaper generated considerably higher particle number concentrations (about 3.0 times) and respirable mass concentrations (about 2.8 times) compared to P180 (Table 1), showing statistically significant differences for all composites (all p-values <0.0001; results not shown). For the size distributions by number (Fig. 4), P100 and P180 generated similar distribution patterns regardless of

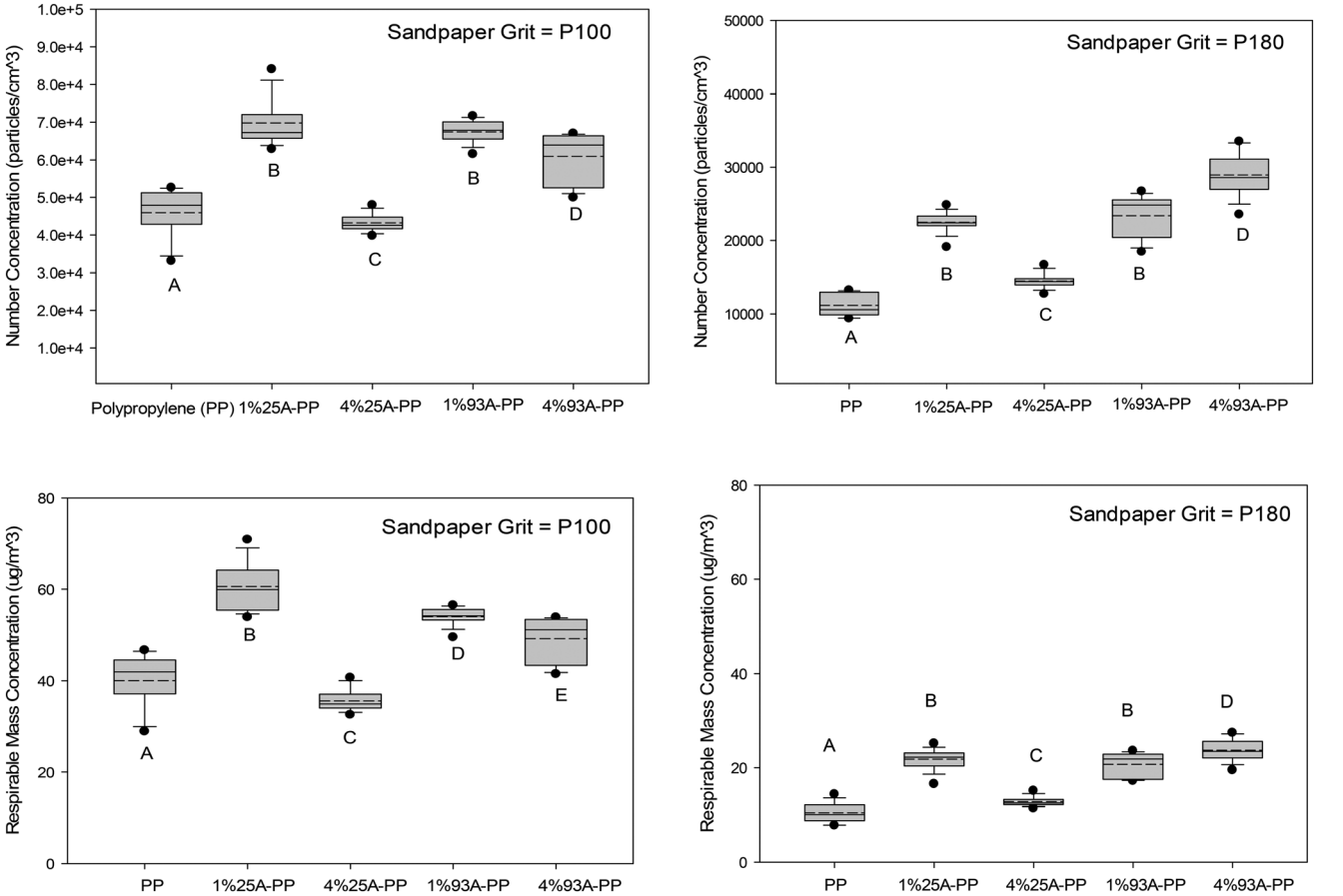

Fig. 3 Particle number concentrations (top row) and respirable mass concentrations (bottom row) by sandpaper type. Each box plot represents 10th, 25th, 50th (median), 75th, and 90th percentiles and the solid circles indicate the 5th (lower) and 95th (upper) percentiles (dashed line = mean). Different letters (A–E) indicate statistically significant differences ($p < 0.05$).

composite type, showing the majority of particles <30 nm with the peak concentrations <15 nm for all testing materials. The results of size distributions by mass revealed most of the mass in particles >10 μm for both sandpapers, although the diameters of peak mass concentrations were different between P100 and P180 (Fig. 4).

2.2 Effects of nanocomposite materials. Particle number and respirable mass concentrations were substantially increased with the addition of 1% 25A, 1% 93A, and 4% 93A nanoclays compared to the virgin PP material for both sandpaper grits, while the addition of 4% 25A showed comparable results to the virgin material (Table 1 and Fig. 3). The number concentrations among different composites revealed statistically significant differences except for the comparisons between 1% 25A-PP and 1% 93A-PP for both grits (p-value = 0.999 for P100 and 0.2399 for P180) and the respirable mass comparisons between 1% 25A-PP and 1% 93A-PP (p-value = 0.7731) for P180.

The peak number concentrations of 1% 25A-PP, 1% 93A-PP, and 4% 93A-PP were considerably higher than those of 4% 25A-PP and PP, reflecting higher total number concentrations (Fig. 4). Conversely, the PP and 4% 25A-PP distributions showed similar shapes and peak number concentrations. Although the diameters of peak number concentrations were slightly different among composites, all peaks happened at <15 nm and no dramatic shift of diameter was observed for the nanocomposites compared to the PP. The particle size distributions by mass were dominated by a single mode with a few exceptions. Minor secondary modes were observed when sanding PP and 4% 93A-PP (peak at ~10 μm) using P100 (Fig. 4C) and 1% 25A-PP (peak at ~4.5 μm) using both P100 and P180 (Fig. 4C and D).

As shown in Fig. 5, overall, particle releases are positively associated with the amount of composite abraded from sanding (r_p = 0.972 for P100 and 0.817 for P180). Also, the particle number concentrations were correlated positively with the tensile strength and toughness (high for P100 and moderate for P180), negatively with the elongation at break (moderate for P100 and low for P180), and poorly with the Young's modulus (Fig. 6 and S2†).

3. MOUDI and temperature variation

Regardless of the sandpaper type and composite materials, >90% of particles were collected on the first MOUDI stage (18.4 μm cut-off) and the remaining stages showed no

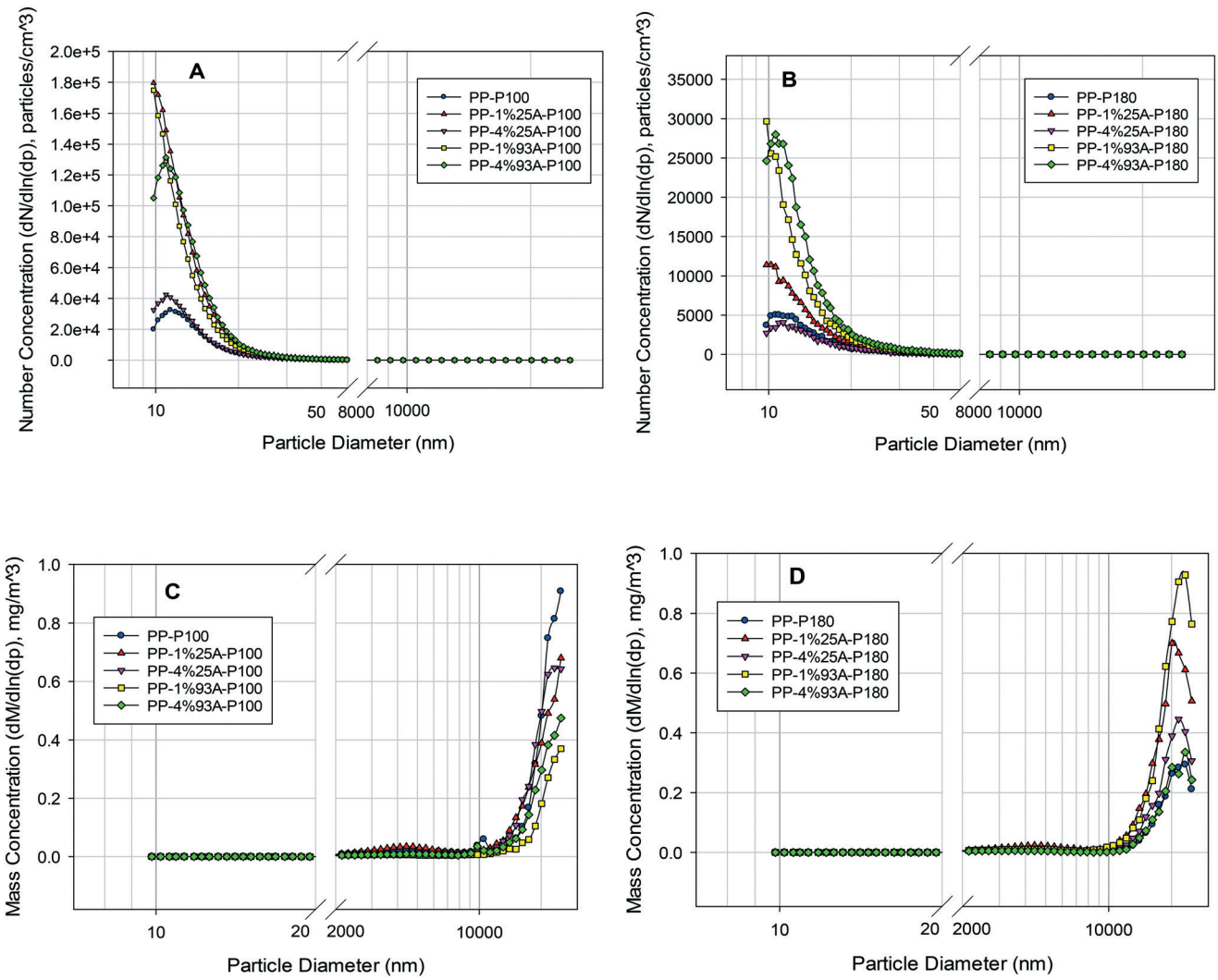

Fig. 4 Particle size distributions by number (A and B) and mass (C and D) concentrations for airborne particulate following sanding of nanoclay-enabled polypropylene composite. Percentages indicate amount of incorporated nanoclay by weight basis.

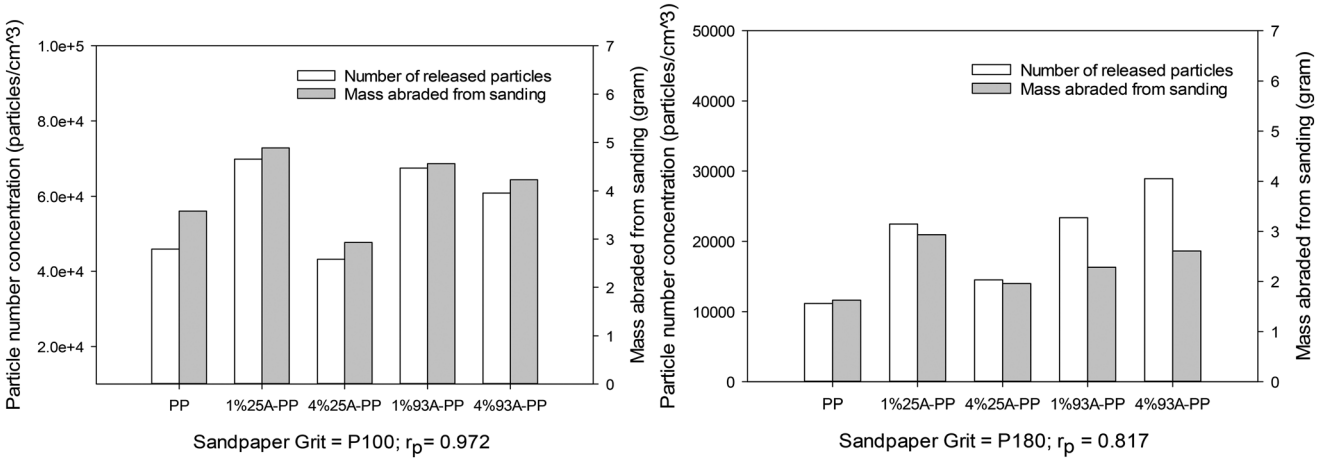

Fig. 5 Comparison of particle number concentrations with the mass of nanoclay-enabled polypropylene composite abraded during sanding. r_p = Pearson correlation coefficient.

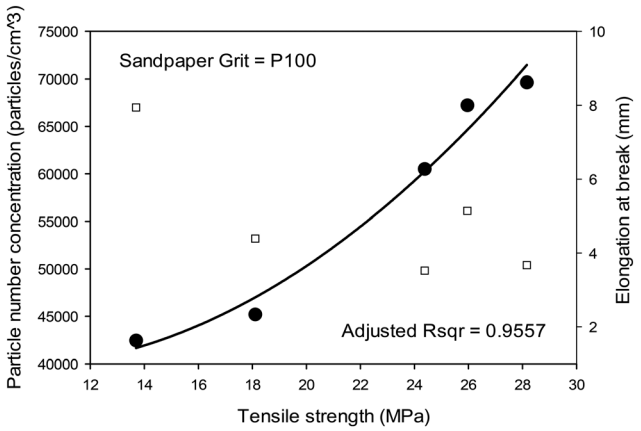

Fig. 6 Relationship of tensile strength with particle number concentrations (solid circles) and elongation at break (open squares). Pearson correlation coefficient (r_p) was 0.978 between tensile strength and particle number and (−0.623) for elongation at break, respectively.

measurable amounts of particles. Thus, no quantitative mass concentrations were calculated using the MOUDI data. Prior to sanding, the temperature measured at the sandpaper in the exposure chamber ranged from 23 to 26 °C (average = 25 °C). The temperature measured after 22 min sanding ranged from 28 to 32 °C (ESI† Table S3).

4. Electron microscopy evaluation

Field blank samples of the IOM filters and TPS100 grids confirmed no cross-contamination between test runs. For all composites, TPS100 samples were very lightly loaded and showed no presence of free nanoclay particle. Additional TEM analysis conducted on filter samples confirmed that the majority of the released particles measured sub-micron in diameter with variable morphologies among the particles observed (ESI† Fig. S4). The sample was subsequently examined in the FESEM, and one free particle of Cloisite 25A during sanding of 1% 25A-PP was observed (Fig. 7). The combined results of TPS100 and FESEM analyses implicate that minimal nanoclay particles generate during sanding,

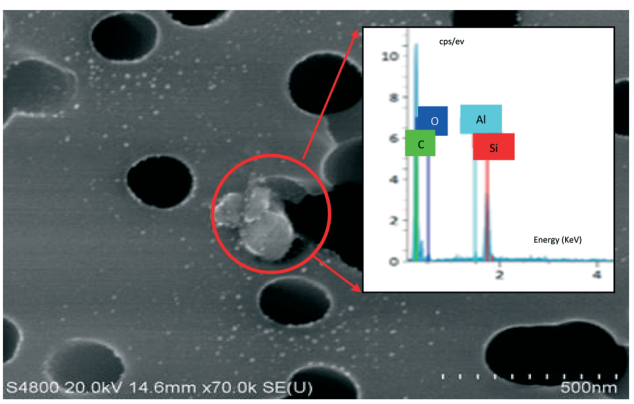

Fig. 7 Secondary electron image and EDS of a free particle of Cloisite 25A collected during sanding of 1% 25A-PP.

indicating that the Cloisite particle found was an isolated occurrence.

The elemental composition and morphology of the collected sanding dust was examined to determine whether a particle was consistent with composite or sandpaper materials. Overall, the composite particles have a smooth surface texture and rounded edges with morphological characteristics that can be differentiated from the particles observed in the sandpaper only sample (ESI† Fig. S5). Inorganic particles associated with the samples were primarily sandpaper debris.

As shown in Table 2, the relative concentration of particle elemental composition by number showed that the P100 sandpaper only sample collected without composite material consisted primarily of C-rich (36% by number%), Na–F–Al (23%), Al–Zr (11%), and Ca-rich (8.6%) particles. The number of composite particles was minor on each sample (4% 93A-PP [2.9%], 4% 25A-PP [2.5%], 1% 25A-PP [2.4%] and 1% 93A-PP [1.9%]), and the virgin PP sample contained 11% by number of PP particles. For each composite material and sandpaper, average elemental compositions for each classification are listed in ESI† Table S4. These results suggest that most particles ≥1 μm captured on the filter were generated by the degradation of sandpaper.

Fig. 8A shows an example of size distribution frequency by number for 4% 93A-PP, demonstrating that the sandpaper particles were in the smaller size fraction than the particles released from the composite. Other nanoclay composite and virgin materials showed similar patterns (ESI† Fig. S6). About 80% by number of non-composite particles measured 1–4 μm in size regardless of the type of nanoclay and concentration used for the composite. Conversely, both 1% nanoclay PP composites displayed about 30% by number of released composite particles in the 1–4 and 4–8 μm size ranges, respectively, suggesting 56–63% of released composite particles within the respirable particle fraction. The 4% nanoclay PP composites showed a decrease in overall size with about 40% of the released particles in the 1–4 μm size range.

Weight percent analysis showed that P100 sandpaper was comprised of particles classified as Na–F–Al (25%), Al–Zr (22%), C-rich (18%), and other (30%) particulate (Table 2). Sanding of composite material resulted in a large shift in mass favoring composite particulate, ranging 66% to 83%, with <15% for all other particulate except for 1% 25A-PP. The size distribution frequency by weight for 4% 93A-PP showed that the vast majority of the sample weight was comprised of composite particles measuring >40 μm (Fig. 8B). The weight percent of 4% 25A-PP and 1% 93A-PP demonstrated similar patterns, indicating that the mass of released particles from composites were dominated by the inhalable fraction of particles (ESI† Fig. S7). Conversely, 1% 25A-PP and PP exhibited the weight percent spread into various particle sizes, while the other nanocomposites showed one distinctive peak at >40 μm. For example, the

Table 2 Summary of particle analysis by number and weight percent (particles ≥ 1 μm; P100 sandpaper)

	Number percent (%)						Weight percent (%)					
	Composite[a]	Al–Zr	Ca-rich	C-rich	Na–F–Al	Other[b]	Composite[a]	Al–Zr	Ca-rich	C-rich	Na–F–Al	Other[b]
Sandpaper	N/A	11	8.6	36	23	21	N/A	22	5.1	18	25	30
PP	11	1.4	43	12	14	19	71	0.6	7.8	15	0.6	5.1
1% 25A-PP	2.4	0.5	39	40	8.2	10	17	0.7	22	52	1.4	6.9
4% 25A-PP	2.5	0.7	30	46	8.0	13	83	0	4.0	11	0.2	1.8
1% 93A-PP	1.9	1.1	39	39	8.6	10	69	0.2	14	14	1.0	1.8
4% 93A-PP	2.9	1.7	49	19	13	14	66	0.5	17	11	1.0	4.5

[a] No elemental composition is reported because nanocomposites are primarily made of carbon and oxygen and have only trace amounts of Al and Si. [b] Includes Al-rich, Zr-rich, C(NaF), Si–Al, Si–Ca, Si-rich, Fe-rich, and miscellaneous; N/A = not available.

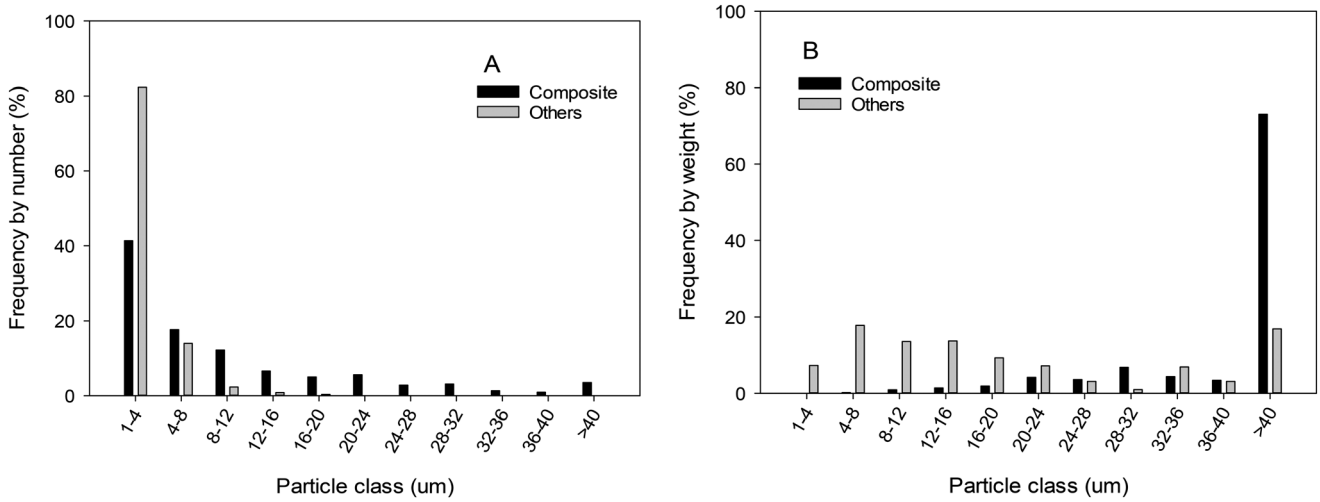

Fig. 8 Size distribution frequency by number (A) and weight (B) for 4% 93A-PP.

weight percent of PP virgin material ranged from ~6–23 wt% for the particle classes of 16–20 μm and above. The 1% 25A-PP showed close to or greater than 5% for all particle classes except for 1–4 μm, 28–32 μm, 32–36 μm, and 36–40 μm (ESI† Fig. S7).

Table 3 presents the evaluation results of particles for nanoplatelet protrusions on nanocomposite particles. The number of particles ≥1 μm per area was the highest for 1% 93A-PP and the lowest for 1% 25A-PP among all nanocomposites. For 25A-PP, 4% composite generated considerably higher number of particles per area, 6.9 times, relative to 1% composite, while the opposite result was observed for 93A-PP (1% showing 1.9 times higher than 4%). The number of composite particles per area showed a similar pattern. Of these, 4% 25A-PP generated the highest percent of composite particles with protrusions (59%) followed by 1% 93A-PP (33%), 4% 93A-PP (27%), and 1% 25A-PP (18%). Fig. 9 shows an example of a FESEM secondary electron image of a particle with protrusions, with traceable Al–Si. Interestingly, we observed numerous sulfur platelets during the CCSEM evaluation in the virgin and nanocomposite materials (Fig. 9). ESI† Fig. S8 shows representative diversity of nanocomposite particulate with and without nanoclay protrusions.

Table 3 CCSEM evaluation of particles analyzed for nanoplatelet protrusions on nanocomposite particles (particles ≥ 1 μm; P100)

Material type	Total particles analyzed	Particles per area (P cm^{-2})	Composite particles	Composite particles per area (P cm^{-2})	Composite particles relocated for protrusion examination	Particles with protrusions	Percent of composite particles with protrusions
1% 25A-PP	3950	1.6×10^4	209	3.91×10^2	209	37	18%
4% 25A-PP	4049	1.1×10^5	214	2.62×10^3	214	126	59%
1% 93A-PP	4912	2.1×10^5	234	4.05×10^3	200	66	33%
4% 93A-PP	3059	1.1×10^5	202	3.31×10^3	202	54	27%

CCSEM = computer-controlled scanning electron microscopy.

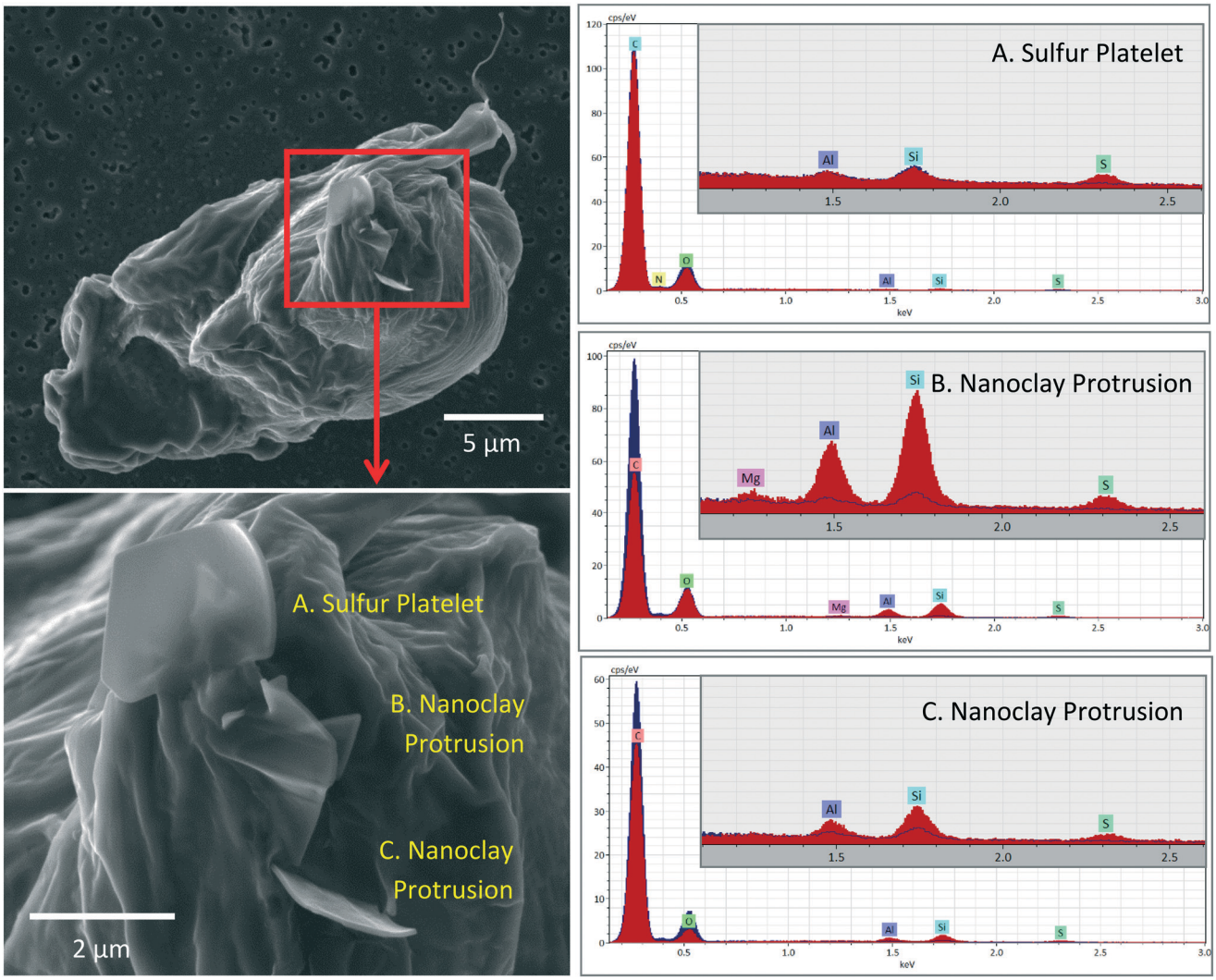

Fig. 9 Secondary electron images and EDS of a sanding composite particle with protrusions (4% 93A-PP). The composite particle EDS (blue) and protrusion/platelet EDS (red) overlays distinguish EDS counts related to platelet features from the composite particle background counts.

Discussion

Concerns with unknown risks have recently arisen surrounding high levels of airborne dusts associated with nanoclay-enabled nanocomposites in occupational settings[35] in part due to the increasing rise in diverse uses of nanoclay-enabled thermoplastic composites across numerous nanotechnologies. This study set out to evaluate the release of airborne particulate during machining from a set of nanoclay-enabled polypropylene composites to investigate how the properties of nanoclay composite affect the size, mass, and chemistry of released dusts.

P100 sandpaper released substantially more particles than P180, with no shift in diameter of peak concentrations for all composites. This is expected because P100 has rougher surface than P180, generating more abrasion of a material than P180. This result was consistent with previous studies[40,56] sanding carbon-nanotube-enabled composites. In contrast, Nored *et al.*[57] reported an opposite result for the aerosolized paint dust generated from manual sanding of coated wood surfaces with TiO_2 (3.2% w/w) when testing with P40, P120, and P220. This difference could be attributed to the type of base matrix material (*i.e.* thermoplastic *vs.* hard cellulose) or differences in applied force (constant controlled *vs.* inconsistent manual) to each material.

For the size distributions by mass, the slight shift of the diameter of peak mass concentration towards the smaller size for P180 than that for P100 can be explained by the rough surface of P100, triggering larger particles than P180 (Fig. 5). For the respirable mass concentrations, P100 produced higher concentrations than P180 (Table 1). This finding is consistent with that reported by Chung *et al.*[58] (P80 *vs.* P180). Kang *et al.*[40] compared P150 and P320 by sanding CNT-enabled composites with various base materials (glass fiber/epoxy resin, acrylonitrile butadiene styrene [ABS], and ABS with carbon black) and reported that the respirable mass concentrations using P150 were not always higher than those using P320. Huang *et al.*[56] tested P80, P150, and P320

by sanding CNT-enabled composites and reported an opposite result as we observed here. In the present study, the shapes of size distributions by mass of P100 and P180 were almost identical for the respirable fractions for all materials. Finer sandpaper than P180 might generate more respirable particles.

Overall, compared to the virgin PP, the addition of both Cloisites generated considerably higher particle number concentrations except for that of 4% 25A (Table 1 and Fig. 3). The mass of material abraded during sanding found that it is highly associated with the released number of particles for all composites (Fig. 5). The present study and a study by Neubauer *et al.*[59] observed a positive correlation between the particle release rate and tensile strength. These findings indicate that the positive relationship between two factors seemed to be a universal occurrence across different matrices and nanomaterials (*e.g.* TPU–CNT, TPU, and TPU–CB by Neubauer *et al.*[59] and five composites here). In addition, we observed that the particle sizes of nanocomposites shifted from large to small as the tensile strength increased (Fig. S6†). Interestingly, the tensile strength of 4% 25A-PP (13.7 MPa) was considerably lower than that of the other nanocomposites showing >24 MPa. Similarly, Young's modulus was also decreased compared to all other composites. This might be related to the degree of dispersion of Cloisite 25A (4% w/w) in the PP. Song and Youn[60] reported that composites with well-dispersed CNTs showed increased tensile strengths as the percentage of CNTs increased, while poorly dispersed CNT composites showed no pattern of tensile strengths. Similar findings were reported for different types of thermoplastic composites with nanoclay as a filler material since overloading or poor dispersion of nanoclay reduced nanoclay/polymer interactions, thereby decreasing composite stiffness.[61,62] In the present study, poorer dispersion of 4% 25A in the PP compared to 4% 93A (Fig. 2) might be the reason for lower particle emission rate compared to 4% 93A-PP. An inverse relationship between the released particle numbers and elongation at break was observed (Fig. 6), which is consistent with that by Hirth *et al.*[63]

All composites showed the peak number concentrations <15 nm and the majority of particles < 30 nm, without noticeable shift of the diameter of peak concentration when added nanoclay materials (Fig. 5). Previous studies[37,64,65] stated that smaller particles (ranging up to sub-100 nm) from sanding were generated from the degradation of sandpaper, not from composites. Although detailed EM analysis was not conducted for particles <30 nm, the results of this study support the findings of previous studies. For example, <12% of composite particles by number (Table 2) and a substantially higher number percent of sandpaper particles in the particle class of 1–4 μm compared to the percent of composite particles (Fig. S6†) imply that the majority of particles with small sizes were generated from the sandpaper, rather than from the composites.

For all composites, size distributions by mass revealed that most of the mass was dominated by the inhalable fraction (Fig. 4 and S7†). The respirable mass concentrations of composites were in the same order as the total particle number concentrations. For P100, 1% 25A-PP generated the highest respirable mass concentrations. This can be supported by the combined results of the smallest number of particles per area (Table 3) and noticeable weight percent at smaller particle sizes (up to 12 μm; Fig. S7†), compared to that of the other composites. Note that particles greater than 10 μm but smaller than 12 μm (*i.e.* beyond the respirable size range) were included in the size distribution by weight percent. Especially, the other three nanocomposites showed one high weight percent at particle size >40 μm. Although no results of CCSEM analysis were available for P180, it is expected to generate the highest respirable mass concentrations of 4% 93A-PP with similar explanation aforementioned for P100.

Huang *et al.*[56] reported that as the weight percent of CNTs increased, the stiffness of the nanocomposite increased, breaking the object into small particles during sanding, and led to the increase of respirable mass concentration. The present study showed inconsistent results. Indeed, an interesting trend was observed in that, for P100 and P180 grit sanding, the amount of and spacing of nanoclay within the matrix correlated with the respirable mass concentrations. For example, virgin PP displayed the smallest peak for respirable particles and addition of nanoclay caused an increase in respirable particle number. This trend was most apparent for the 1% nanoclay-enabled composites and the better dispersed 4% 93A composite. The poorly dispersed 4% 25A composite trended with virgin PP composite.

Interestingly, 4% 25A-PP showed higher number percent of size distributions in large particle classes compared to the other nanocomposites (Fig. S6†). During the manual examination of nanoclay protrusion, the analyst noted that protrusions were more common in large particle structures compared to small particles, probably due to largely observable surface area on a per particle basis. This might be a reason why we observed the highest percent of protrusions in 4% 25A-PP (59%) composite particulate compared to other nanocomposites. In addition, poorly dispersed 4% 25A in the PP resulted in more agglomerated particles within the matrix compared to the 4% 93A-PP, resulting in detectable large protruding agglomerated nanoclay in released composite particulate. Similarly, but in the opposite direction, 1% 25A-PP revealed higher number percent in small particle classes compared to other nanocomposites (Fig. S6†) and resulted in the lowest percent of protrusions (18%) among the other nanocomposites. Poorly dispersed nanoclay with large spaces between nanoclay agglomerates would result in a low percentage of protrusions following matrix breakdown. It is expected to have more nanoclay particles per area for 4% Cloisite mixed in the PP compared to 1% Cloisite. However, Cloisite 93A showed a contrary result, leading to the percent of composite particles with protrusions of 33% (1% 93A-PP) and 27% (4% 93A-PP). The difference might be related to the degree of dispersion of nanoclay in the PP and mechanical

properties. ESI† Fig. S6 also supports this observation demonstrating that 1% showed larger particle sizes than 4%.

We observed a free particle of Cloisite 25A on a filter sample from sanded 1% 25A-PP (Fig. 7), probably from poorly dispersed Cloisite 25A in the polymer, breaking a free particle from agglomerates. For the other nanocomposites, no free particles of nanoclay were observed. In addition, numerous sulfur platelets were observed in the collected particles after sanding for all composites. Indeed, the sulfur was found in the bulk PP pellets prior to making a composite. Xiong *et al.*[66] reported that sulfur was used to speed up the cooling of the PP composite synthesis and demonstrated no impact of added sulfur on the crystallization of PP when compared XRDs of the neat PP, sulfur, and PP/sulfur blends (3%, 5%, and 10% sulfur). In addition, elemental sulfur was added as a reinforcing agent to improve elongation at break in high density polyethylene with no apparent change in composite quality.[67] Since sulfur has a low melting point (108 °C), it probably melted during the PP composite synthesis and then crystalized in platelet form during the cooling. By comparing the results by Xiong *et al.*[66] (Fig. 1) and this study (Fig. S3†), it is expected that the sulfur content would be <5%.

The findings of this study suggest that the inclusion of nanoclays with different percent loading (0% *vs.* 1% *vs.* 4%) has an effect on the nanocomposite matrix structure and the rate of degradation of the composites (including 1% 25A, 1% 93A, and 4% 93A nanoclays) during sanding. Previous studies[64,68] reported that particle releases were dependent on the rigidity of composite matrix rather than the presence of nanofillers. The present study agreed with those previous studies, indicating that the mechanical properties of composites influenced more the released number of particles than the weight percent of nanoclays in the polymer. Sandpaper grit sizes also influenced the particle number and respirable mass concentrations. In addition, mechanical processing (*i.e.*, sanding) produced airborne particles with protrusions of nanoclay and a free nanoclay particle (for 1% 25A-PP). These findings indicate that higher particle concentrations and/or modification of surface structures of generated airborne particles from nanoclay-enabled PP composite could potentially elicit more severe adverse health effects after inhalation compared to dust from virgin PP alone. Furthermore, our detailed analysis shows that generated dusts following nanocomposite machining is truly a complex particle mixture. At present, a majority of ENM toxicological studies are based on the as-produced material properties, and not with ENM-enabled materials generated during life cycle.[69] However, recent research shows that released particles during the use phase of the life cycle (*e.g.*, mechanical processing, UV and thermal treatment) were mostly dominated by particles with embedded or protruded nanofillers (with a few occurrences of free nanofillers).[40,59,70,71] This study adds to these findings using a 2-dimensional aluminosilicate ENM material and suggests that airborne complex mixture dusts during nanocomposite breakdown may represent an understudied occupational hazard. Thus, evaluating only the ENM particles early in the material's life cycle would not adequately assess potential particle hazards (respirable or inhalable fractions) released from mechanical manipulations of nanocomposites.

The change of temperature before and during sanding, measured at the site where a composite touched the sandpaper, was minimal (Table S3†). This is considerably lower than the PP melting point (130 °C to 171 °C) and thus, no generation of polymer fume was expected due to the thermal degradation of composites. Nevertheless, we cannot fully exclude the possibility of released polymer fume; sample collection to determine (semi) volatile organic compounds, which was not conducted here, might be helpful. The findings of this study were limited to the nanoclay concentrations up to 4% by weight and may not apply to higher filler concentrations or post-modification of released particles.

Conclusions

This study presented that percent loading and dispersion within the polypropylene matrix, along with type of sandpaper, affected nanocomposite material properties, which correlated with released particle size, mass, and chemistry distributions in the inhalable fraction during sanding activities. Given the testing condition of two sandpaper grits and five composites employed in this study, no dramatic changes of shapes for size distributions by number and mass were observed between test conditions; only magnitude of ultrafine and large particle sizes were affected. A free Cloisite 25A particle was observed in airborne samples from sanded 1% 25A-PP composite. The findings of this study indicate that the majority of inhalable particles was from the composite materials (based on the size distributions by number percent) and particles <30 nm from the sandpaper indicative of a complex airborne dust mixture. A significant number of the composite particles displayed platelet-shaped protrusions with a composition and morphology indicative of nanoclay. The findings of this study potentially have implications for occupational hazards of machining nanoclay-enabled composites and on the toxicity of the particles generated as higher particle concentrations and/or modification of surface structures could potentially elicit more severe adverse health effects after inhalation. Currently, *in vivo*/*in vitro* toxicity studies are underway with collected inhalable particle fractions to investigate potential risk of pulmonary diseases.

Conflicts of interest

The findings and conclusions in this report are those of the authors and do not necessarily represent the official position of the National Institute for Occupational Safety and Health, Centers for Disease Control and Prevention. Mention of any company or product does not constitute endorsement by NIOSH/CDC.

Acknowledgements

The authors acknowledge use of WVU Shared Research Facilities. This work was funded by the Nanotechnology Research Center of the National Institute for Occupational Safety and Health (921043X and 921043S) and a CAREER Award from the National Science Foundation (1454230).

References

1 M. S. Nazir, M. H. M. Kassim, L. Mohapatra, M. A. Gilani, M. R. Raza and K. Majeed, in *Nanoclay Reinforced Polymer Composites Nanocomposites and Bionanocomposites*, ed. M. Jawaid, A. E. K. Qaiss and R. Bouhfid, Springer, 2016, pp. 35–55.
2 N. A. Isitman and C. Kaynak, *Polym. Degrad. Stab.*, 2010, **95**, 1759–1768.
3 N. A. Isitman and C. Kaynak, *Polym. Degrad. Stab.*, 2010, **95**, 1523–1532.
4 S. J. Ahmadi, Y. D. Huang and W. Li, *J. Mater. Sci.*, 2004, **39**, 1919–1925.
5 D. R. Paul and L. M. Robeson, *Polymer*, 2008, **49**, 3187–3204.
6 D. A. Pereira de Abreu, P. Paseiro Losada, I. Angulo and J. M. Cruz, *Eur. Polym. J.*, 2007, **43**, 2229–2243.
7 F. C. Udon, *Metall. Mater. Trans. A*, 2008, **39**, 2804–2814.
8 P. Singla, R. Mehta and S. N. Upadhyay, *Green Sustainable Chem.*, 2012, **2**, 21–25.
9 J. P. Schreider, M. R. Culbertson and O. G. Raabe, *Environ. Res.*, 1985, **38**, 256–274.
10 S. M'anyai, J. Kabai, J. Kis, E. Suveges and M. Timar, *Med. Lav.*, 1969, **60**, 331–342.
11 D. W. Oscarson, G. E. Van Scoyoc and J. L. Ahlrichs, *J. Pharm. Sci.*, 1981, **70**, 657–659.
12 I. P. Gormley and J. Addison, *Clay Miner.*, 1983, **18**, 153–163.
13 I. P. Gormely, M. J. Kowolik and R. T. Cullen, *Br. J. Exp. Pathol.*, 1985, **66**, 409–416.
14 E. J. Murphy, E. Roberts and L. A. Horrocks, *Neuroscience*, 1993, **55**, 597–605.
15 E. J. Murphy, E. Roberts, D. K. Anderson and L. A. Horrocks, *Neuroscience*, 1993, **57**, 483–490.
16 A. Wagner, A. P. White, T. A. Stueckle, D. Banerjee, K. A. Sierros, Y. Rojanasakul, S. Agarwal, R. K. Gupta and C. Z. Dinu, *ACS Appl. Mater. Interfaces*, 2017, **9**, 32323–32335.
17 A. Wagner, R. Eldawud, A. White, S. Agarwal, T. A. Stueckle, K. A. Sierros, Y. Rojanasakul, R. K. Gupta and C. Z. Dinu, *Biochim. Biophys. Acta*, 2017, **1861**, 3406–3415.
18 N. K. Verma, E. Moore, W. Blau, Y. Volkov and P. R. Babu, *J. Nanopart. Res.*, 2012, **14**, 1–11.
19 G. Janer, E. Fernández-Rosas, E. Mas del Monlino, D. González-Gálvez, G. Vilar, C. López-Iglesias, V. Ermini and S. Vázquez-Campos, *Nanobiotechnology*, 2014, **8**, 279–294.
20 S. Lordan, J. E. Kennedy and C. L. Higginbotham, *J. Appl. Toxicol.*, 2011, **31**, 27–35.
21 M. Baek, J. Lee and S. Choi, *Mol. Cell. Toxicol.*, 2012, **8**, 95–101.
22 S. Maisanaba, K. Hercog, N. Ortuño, A. Jos and B. Zegura, *Chemosphere*, 2016, **154**, 240–248.
23 M. Zhang, X. Li, Y. Lu, X. Fang, Q. Chen, M. Xing and J. He, *Mutat. Res.*, 2011, **720**, 62–66.
24 J. Houtman, S. Maisanaba, M. Puerto, D. Gutièrrez-Praena, M. Jordá, S. Aucejo and A. Jos, *Appl. Clay Sci.*, 2014, **90**, 150–158.
25 D. R. Lewis, *Proceedings of the First National Conference on Clays and Clay Technology*, University of California, Berkeley, 1955, vol. 169, pp. 54–69.
26 P. M. S. Souza, A. R. Morales, M. A. Marin-Morales and L. H. I. Mei, *J. Polym. Environ.*, 2013, **21**, 738–759.
27 L. Roes, M. K. Patel, E. Worrell and C. Ludwig, *Sci. Total Environ.*, 2012, **417–418**, 76–86.
28 J. S. Lighty, J. M. Veranth and A. F. Sarofim, *J. Air Waste Manage. Assoc.*, 2000, **50**, 1565–1618.
29 P. H. Hoet, I. Brüske-Hohlfeld and O. V. Salata, *J. Nanobiotechnol.*, 2004, **2**(12), 1–15.
30 S. Bakand, A. Hayes and F. Dechsakulthorn, *Inhalation Toxicol.*, 2012, **24**, 125–135.
31 T. A. Stueckle, D. C. Davidson, R. Derk, T. G. Kornberg, L. Battelli, S. Friend, M. Orandle, A. Wagner, C. Z. Dinu, K. A. Sierros, S. Agarwal, R. K. Gupta, Y. Rojanasakul, D. W. Porter and L. Rojanasakul, *ACS Nano*, 2018, **12**, 2292–2310.
32 T. Kuhlbusch, C. Asbach, H. Fissan, D. Göhler and M. Stintz, *Part. Fibre Toxicol.*, 2011, **8**, 1–18.
33 L. Schlagenhauf, F. Nüesch and J. Wang, *Fibers*, 2014, **2**, 108–127.
34 S. J. Froggett, S. F. Clancy, D. R. Boverhof and C. A. Richard, *Part. Fibre Toxicol.*, 2014, **11**(17), 1–28.
35 A. Mackevica and S. F. Hansen, *Nanotoxicology*, 2016, **1**, 1–3.
36 P. Raynor, J. Cebula, J. Spangenberger, B. Olson, J. Dasch and J. D'Arcy, *J. Occup. Environ. Hyg.*, 2012, **9**, 1–13.
37 S. Sachse, F. Silva, H. Zhu, A. Irfan, A. Leszczynska, K. Pielichowski, V. Ermini, M. Blazquez, O. Kuzmenko and J. Njuguna, *J. Nanomater.*, 2012, **2012**(189386), 1–8.
38 C. S. J. Tsai, D. White, H. Rodriguez, C. E. Munoz, C. Huang, C. Tsai, C. Barry and M. J. Ellenbecker, *J. Nanopart. Res.*, 2012, **14**(989), 1–14.
39 A. Guiot, L. Golanski and F. Tardif, *J. Phys.: Conf. Ser.*, 2009, **170**, 012014.
40 J. Kang, A. Erdely, A. Afshari, G. Casuccio, K. Bunker, T. Lersch, M. M. Dahm, D. Farcas and L. Cena, *NanoImpact*, 2017, **5**, 41–50.
41 A. L. Roes, E. Marsili, E. Nieuwlaar and M. K. Patel, *J. Polym. Environ.*, 2007, **15**, 212–226.
42 A. Wagner, A. P. White, M. C. Tang, S. Agarwal, T. A. Stueckle, Y. Rojanasakul, R. K. Gupta and C. Z. Dinu, *Sci. Rep.*, 2018, **8**(10709), 1–15.
43 D. Leigh, D. Miller-Lionberg, G. Casuccio, T. Lersch, H. Lentz, A. Marchese and J. Volckens, *Aerosol Sci. Technol.*, 2014, **48**, 81–89.
44 W. C. Hinds, in *Aerosol Technology, Properties, Behavior, and Measurement of Aerosol Particles*, John Wiley & Sons Inc., New York, 2nd edn, 1999, ch. 3, pp. 53–54.
45 J. E. Bonevich and W. K. Haller, *NIST-NCL Joint Assay Protocol, PCC-7 Version. 1*, 2010.
46 T. M. Peters, E. J. Sawvel, R. Willis, R. R. West and G. S. Casuccio, *Environ. Sci. Technol.*, 2006, **50**, 7581–7589.

47 A. D. Maynard and P. A. Jensen, in *Aerosol Measurement: Principles, Techniques, and Applications*, ed. P. Baron and K. Willeke, John Wiley & Sons Inc., New York, 2nd edn, 2005, pp. 779–799.
48 K. Chrissopoulou and S. H. Anastasiadis, *Eur. Polym. J.*, 2011, **47**, 600–613.
49 T. Nishino, T. Matsumoto and K. Nakamae, *Polym. Eng. Sci.*, 2000, **40**, 336–343.
50 R. P. Dwivedi, A. K. Gupta, B. S. Mohanty and S. K. Nayak, *Int. J. Sci. Eng. Appl. Sci.*, 2015, **1**, 2395–3470.
51 R. Pal, H. N. N. Murthy, K. S. Rai and M. Krishna, *Int. J. ChemTech Res.*, 2014, **6**, 916–928.
52 W. Liu, S. V. Hoa and M. Pugh, *Compos. Sci. Technol.*, 2005, **65**, 2364–2373.
53 M. Abdollahi, M. Rezaei and G. Farzi, *J. Food Eng.*, 2012, **111**, 343–350.
54 J. Rhim, S. Hong and C. Ha, *LWT–Food Sci. Technol.*, 2009, **42**, 612–617.
55 S. Kim, E. A. Lofgren and S. A. Jabarin, *J. Appl. Polym. Sci.*, 2013, 2201–2212.
56 G. Huang, J. H. Park, L. G. Cena, B. L. Shelton and T. M. Peters, *J. Nanopart. Res.*, 2012, **14**(1231), 1–13.
57 A. W. Nored, G. C. Marie-Cecile and I. G. Kavouras, *J. Occup. Environ. Hyg.*, 2018, **9**, 629–640.
58 K. Y. K. Chung, R. J. Cuthbert, G. S. Revell, S. G. Wassel and N. Summers, *Ann. Occup. Hyg.*, 2000, **44**, 455–466.
59 N. Neubauer, W. Wohlleben and Ž. Tomović, *J. Nanopart. Res.*, 2017, **19**(112), 1–15.
60 Y. S. Song and J. R. Youn, *Carbon*, 2005, **43**, 1378–1385.
61 D. J. Daniel and K. Panneerselvam, *Trans. Indian Inst. Met.*, 2017, **70**, 1131–1138.
62 N. Domun, H. Hadavinia, T. Zhang, T. Sainsbury, G. H. Liaghat and S. Vahid, *Nanoscale*, 2015, **7**, 10294–10329.
63 S. Hirth, L. Cena, G. Cox, Z. Tomovic, T. Peters and W. Wohlleben, *J. Nanopart. Res.*, 2013, **15**(1504), 1–15.
64 W. Wohlleben, S. Brill, M. W. Meier, M. Mertler, G. Cox, S. Hirth, B. von Vacano, V. Strauss, S. Treumann, K. Wiench, L. Ma-Hock and R. Landsiedel, *Small*, 2011, **16**, 2384–2395.
65 I. K. Koponen, K. A. Jensen and T. Schneider, *Proceedings of the Inhaled Particles X*, Manchester, 2009.
66 J. Xiong, D. P. Gong, Y. M. Sun and X. P. Zhao, *Polym.-Plast. Technol. Mater.*, 2019, **58**, 1342–1353.
67 K. K. Jena and S. M. Alhassan, *J. Appl. Polym. Sci.*, 2016, **133**(43060), 1–14.
68 D. Göhler, M. Stintz, L. Hillemann and M. Vorbau, *Ann. Occup. Hyg.*, 2010, **54**, 615–624.
69 R. Landsiedel, L. Ma-Hock, K. Kroll, D. Hahn, J. Schnekenburger, K. Wiench and W. Wohlleben, *Adv. Mater.*, 2010, **22**, 2601–2627.
70 B. Nowack, R. M. David, H. Fissan, H. Morris, J. A. Shatkin, M. Stintz, R. Zepp and D. Brouwer, *Environ. Int.*, 2013, **59**, 1–11.
71 C. Kingston, R. Zepp, A. Andrady, D. Boverhof, R. Fehir, D. Hawkins, J. Roberts, P. Sayre, B. Shelton, Y. Sultan, V. Vejins and W. Wohlleben, *Carbon*, 2014, **68**, 33–57.